FRONTIERS OF PHYSICS

RESEARCH ARTICLE
Volume 19 / Issue 3 / 33212 / 2024

Stable alkali halide vapor assisted chemical vapor deposition of 2D $HfSe_2$ templates and controllable oxidation of its heterostructures

Wenlong Chu[1], Xilong Zhou[1], Ze Wang[2], Xiulian Fan[1], Xuehao Guo[1,3], Cheng Li[1], Jianling Yue[2], Fangping Ouyang[1,2,3], Jiong Zhao[4], Yu Zhou[1,2,†]

1 School of Physics, Hunan Key Laboratory of Nanophotonics and Devices, Central South University, Changsha 410083, China
2 State Key Laboratory of Powder Metallurgy, Central South University, Changsha 410083, China
3 School of Physical Science and Technology, Xinjiang University, Urumqi 830046, China
4 Department of Applied Physics, The Hong Kong Polytechnic University, Kowloon, Hong Kong, China
Corresponding author. E-mail: †yu.zhou@csu.edu.cn
Received April 1, 2024; accepted April 20, 2024

ABSTRACT

Two-dimensional hafnium-based semiconductors and their heterostructures with native oxides have been shown unique physical properties and potential electronic and optoelectronic applications. However, the scalable synthesis methods for ultrathin layered hafnium-based semiconductor laterally epitaxy growth and its heterostructure are still restricted, also for the understanding of its formation mechanism. Herein, we report the stable sublimation of alkali halide vapor assisted synthesis strategy for high-quality 2D $HfSe_2$ nanosheets via chemical vapor deposition. Single-crystalline ultrathin 2D $HfSe_2$ nanosheets were systematically grown by tuning the growth parameters, reaching the lateral size of 6–40 μm and the thickness down to 4.5 nm. The scalable amorphous HfO_2 and $HfSe_2$ heterostructures were achieved by the controllable oxidation, which benefited from the approximate zero Gibbs free energy of unstable 2D $HfSe_2$ templates. The crystal structure, elemental, and time dependent Raman characterization were carried out to understand surface precipitated Se atoms and the formation of amorphous Hf–O bonds, confirming the slow surface oxidation and lattice incorporation of oxygen atoms. The relatively smooth surface roughness and electrical potential change of HfO_2–$HfSe_2$ heterostructures indicate the excellent interface quality, which helps obtain the high performance memristor with high on/off ratio of 10^5 and long retention period over 9000 s. Our work introduces a new vapor catalysts strategy for the synthesis of lateral 2D $HfSe_2$ nanosheets, also providing the scalable oxidation of the Hf-based heterostructures for 2D electronic devices.

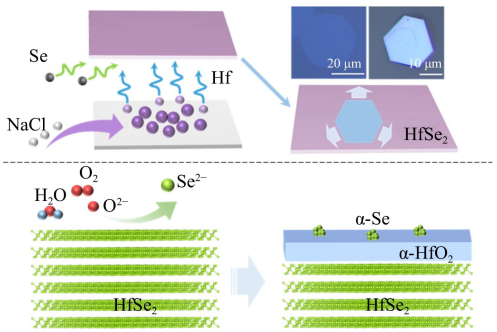

Keywords chemical vapor deposition, $HfSe_2$–HfO_2, nanoelectronics

1 Introduction

Two-dimensional transition metal chalcogenides have been demonstrated with high carrier mobilities [1], polarization switchable ferroelectricity [2] and tunable magnetic properties of ferromagnetism [3–6], spin glass

Higher Education Press

https://doi.org/10.1007/s11467-024-1414-7

state [7] and specific surface area with high reaction ability down to monolayer limit [8, 9], thus booming in the potential applications of electronic, optoelectronic, magnetic, catalytic conversion and storage devices [4, 10–20]. Different from MoS_2 and ReS_2 material families with weak interlayer interaction, layered hafnium chalcogenides (HfS_2 and $HfSe_2$) share much stronger van der Waals force, resulting in the extreme difficulty for the exfoliation and bottom-up synthesis of ultrathin 2D layers [21]. Meantime, layer dependent moderate bandgap from bulk to monolayer of 1.13–1.18 eV for $HfSe_2$, is similar with traditional silicon semiconductor for transistor channel application [22]. The theoretical band structure calculation also has predicted $HfSe_2$ with high phonon-limited mobility of 3500 $cm^2 \cdot V^{-1} \cdot s^{-1}$, which is nearly 10 times higher than that of the extensively studied MoS_2 (340 $cm^2 \cdot V^{-1} \cdot s^{-1}$) [23]. The electronic transport prediction for 2D $HfSe_2$ field effect transistors demonstrated the record on-state current density of 5000 $\mu A \cdot \mu m^{-1}$ (about 650 times that of MoS_2) [24]. Moreover, high dielectric constant HfO_2 is a compatible oxide of 2D $HfSe_2$, which could be achieved by the slow oxidation process similar to the Si/SiO_2 and Bi_2O_2Se/Bi_2SeO_5 interface [1, 22, 25]. Therefore, scalable synthesis of layered 2D $HfSe_2$ and its heterostructure should be highly desirable to realize low-power electronic and optoelectronic devices [24].

Most recently, ultrathin exfoliated $HfSe_2$ nanoflakes from chemical vapor transport synthesized singe crystals demonstrated the promising transistor performance (on/off ratio $> 10^6$; on current, 30 $\mu A/\mu m$) due to the interfacial trap free native oxides [22]. Although 2D $HfSe_2$ nanoflakes and their heterostructures have been confirmed with excellent electronic device performance, scalable synthesis of large area 2D $HfSe_2$ nanoflakes and their heterostructures were still rarely reported [22, 26–29]. Low pressure chemical vapor deposition with the utilization of the selenolate complexes $[Cp_2Hf(SeR)_2]$ showed the synthesis of randomly nucleated flower-like nanostructure films [30]. Two-dimensional $HfSe_2$ nanostructures and $MoSe_2/HfSe_2$ van der Waals heterostructures were synthesized by molecular beam epitaxy (MBE), also providing the obvious evidence of an ordered Se adlayer by high-resolution scanning tunneling microscopy characterization [31, 32]. Polycrystalline wafer-scale 2D $HfSe_2$ thin films were achieved by the MBE with the solid supply of Hf and Se, which were also applied to memristor crossbar array for energy-efficient neural network hardware [33]. Randomly vertical oriented HfS_2 nanosheets, polycrystalline small-sized $HfSe_2$ samples, and $HfS_{2(1-x)}Se_{2x}$ alloys were grown by the highly volatile $HfCl_4$ precursors, which are still far from the requirement of electronic devices application in terms of domain size and the lateral flakesgeometry [34–36]. Therefore, the stable synthesis of high-quality 2D single-crystal $HfSe_2$ nanosheets on the diverse substrates laterally is highly desirable, which also could be utilized as scalable oxidation templates for HfO_2–$HfSe_2$ heterostructures, avoiding the nucleation problem of dielectric layer growth on dangling bond free surface [37].

Herein, we report a remote molten salt (NaCl) vapor-assisted stable volatilization of high melting point hafnium-based precursor (HfO_2) for the CVD synthesis of high-quality single-crystal $HfSe_2$ nanosheets and thin films on various substrates. The size (6–40 μm), thickness (~4.5 nm), and shape (hexagonal to circular) of $HfSe_2$ nanosheets can be precisely tuned by varying the growth parameters. High quality HfO_2–$HfSe_2$ heterostructures were formed by the slow natural oxidation, which has been confirmed with clear lattice incorporation of oxygen atoms and the formation of surface amorphous oxide layers. Further, we investigated the natural oxidation process of $HfSe_2$ in air and explored the memristor application of HfO_2–$HfSe_2$ heterostructures. These findings provide a new idea for the scalable synthesis of two-dimensional hafnium-based chalcogenides laterally and demonstrate that the HfO_2–$HfSe_2$ heterostructures hold great promise in the field of information storage devices.

2 Experimental section

2.1 Preparation of $HfSe_2$ nanosheets

Two-dimensional $HfSe_2$ nanosheets were synthesized on Mica, Si/SiO_2 substrates using remote molten salt (NaCl)-assisted volatilization of a high melting point hafnium-based precursor (HfO_2) in an atmospheric pressure chemical vapor deposition system. Specifically, the high melting point hafnium-based precursor (HfO_2, Aladdin, ≥99.9%) was placed in a quartz boat at a high temperature in the center of a tube furnace. The substrate is reversely placed over the precursor. The NaCl (Aladdin, ≥99.5%) powder was placed upstream of the tube furnace at approximately 780 °C. The Se (Aladdin, ≥99.5%) powder was similarly placed upstream of the tube furnace and heated using an external heating band set at 260–340 °C. Before growth, the quartz tube was purged using high-purity argon (Ar), and then the furnace temperature was increased to 780–960 °C and kept constant for 10 min under the argon flow rate of 30 sccm. The specific growth schematic is shown in Fig. 1(a).

2.2 Sample characterization

The optical microscope (OM, OLYMPUS BX53M) has been used to obtain the morphology of the $HfSe_2$ nanosheets. The Raman spectrometer (Raman, Renishaw inVia Reflex) with a 532 nm laser as the excitation source was used to collect spectra of $HfSe_2$

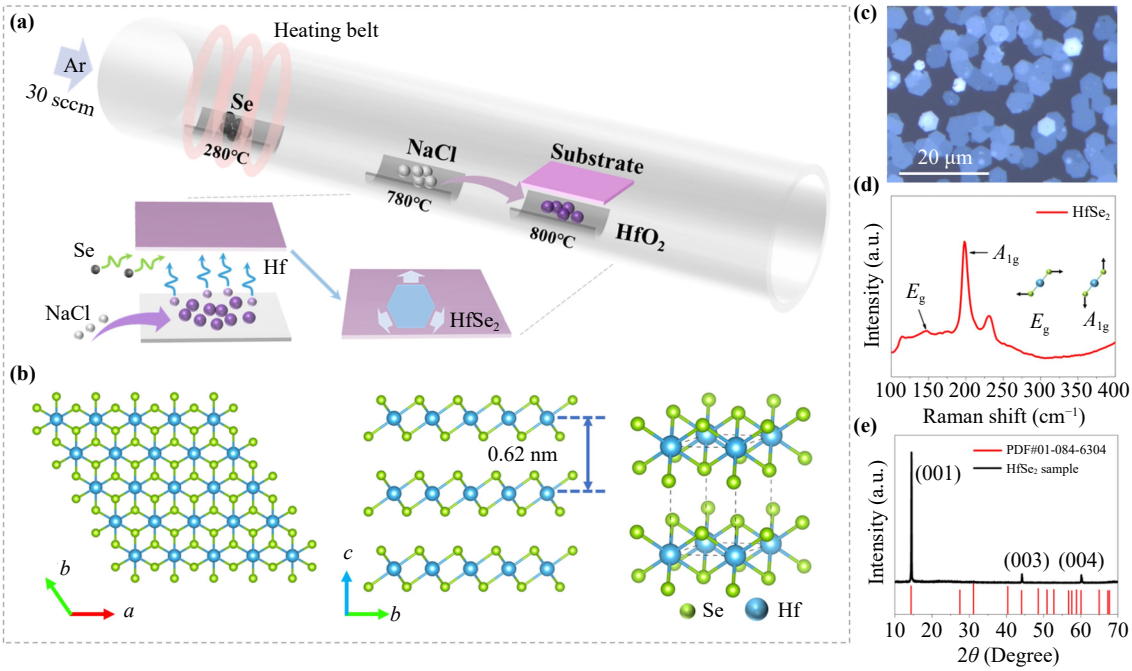

Fig. 1 **(a)** Schematic diagram of remote alkali halide vapor assisted stable sublimation of high melting point hafnium dioxide for controlled synthesis of 2D $HfSe_2$ nanosheets. The NaCl and HfO_2 powder were arranged at the separated temperature of 780 °C, and 800 °C, respectively. **(b)** Schematic atomic structures of 1T-$HfSe_2$ along the ab and bc crystal planes, also for its unit cell. **(c)** Typical optical image of the synthesized $HfSe_2$ nanosheets on the mica substrate. **(d)** Raman spectra and **(e)** XRD pattern of the synthesized $HfSe_2$ nanosheets.

nanosheets to determine molecular vibration bonds of the sample. The crystal structures were characterized by X-ray diffraction (XRD, PERSEE XD-3). The thickness of the sample was determined using an atomic force microscope and the surface potential of the samples was tested using Scanning Kelvin Probe Microscopy (OXFORD MFP-3D Origin). Transmission electron microscopy (TEM, FEI Tecnai F20) is used to analyze the crystal structure and elemental composition of the $HfSe_2$ nanosheets.

2.3 Device fabrication and property measurement

The device is fabricated via an Ultraviolet Maskless Lithography machine (TuoTuo Technology (Suzhou) Co., Ltd.). The naturally oxidized 2D $HfSe_2$ (25 °C, 40% humidity, 48 h) were used to fabricate the devices. The transfer platform was used to transfer the sheet to a specific location. Physical vapor deposition equipment (VNANO VZZ-300S) was used to deposit Cr/Au as electrodes. The memristor properties of the devices were tested by a semiconductor analyzer (PDA FS-Pro) connected with a probe station at room temperature.

3 Results and discussion

To achieve high-quality two-dimensional (2D) $HfSe_2$ nanosheets as the heterostructure template, we propose a remote alkali halide vapor assisted chemical vapor deposition [Fig. 1(a)]. Different from the normal growth using the precursor mixtures, our design strategy separated the location of HfO_2 and NaCl to avoid the precursor supply shortage or erupt [38]. The alkali halide powder was placed around its melting temperature of 780 °C, separately arranging the HfO_2 powers (800–940 °C), which could continuously provide the vapor phase of alkali halide molecule to react with the HfO_2 surface for stable sublimation. The freshly exfoliated mica or SiO_2/Si substrate was settled on the top of HfO_2 powders, in which the reaction species were transported to the substrate surface and formed the nuclei. Thus, the nuclei could epitaxially grow towards in-plane direction to form 2D $HfSe_2$ under the continuous mild supply, avoiding the small sizes or the vertical nanosheets formation [36, 39–41]. Figure 1(b) shows the schematic crystal structure of 1T phase $HfSe_2$ (–4.550 eV), which has a lower formation energy than 2H-$HfSe_2$ (–4.045 eV). In details, 1T-$HfSe_2$ belongs to the hexagonal crystal system with space group of $P\bar{3}m1$, showing the lattice parameters of $a = b = 3.744$ Å, $c = 6.155$ Å, $\alpha = \beta = 90°$, $\gamma = 120°$ [27]. Monolayer 1T-$HfSe_2$ consists of two layers of Se atoms sandwich a layer of Hf atoms with interlayer covalent bonding, in which the Hf atoms are located at the center of an octahedron composed of Se atoms, with a spacing distance of 0.62 nm [Fig. 1(b)] [42].

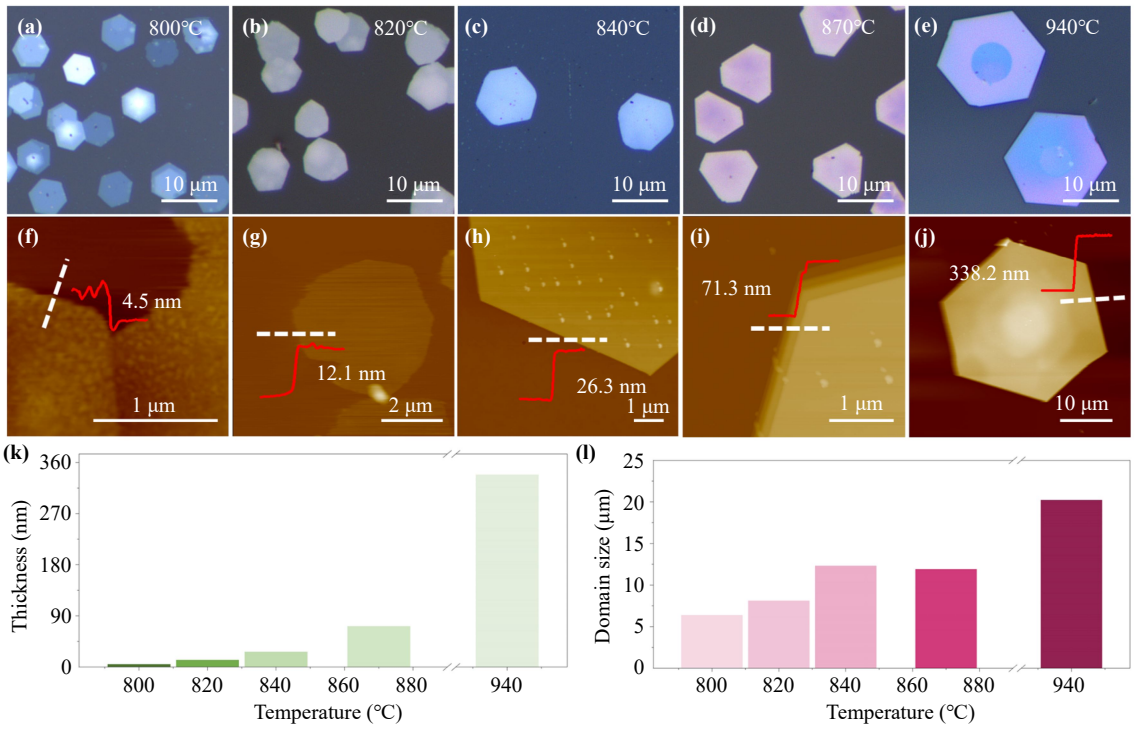

Fig. 2 **(a–e)** Optical images of $HfSe_2$ nanosheets grown on mica substrates at different growth temperatures: 800 °C, 820 °C, 840 °C, 870 °C, and 940 °C, respectively, under the argon flow rate of 30 sccm, Se temperature of 280 °C and growth time of 10 min. **(f–j)** Corresponding representative AFM images. **(k)** Statistical graph of the thickness of $HfSe_2$ nanosheets at different growth temperatures. **(l)** Statistical graphs of $HfSe_2$ nanosheet domain sizes at different growth temperatures.

Figure 1(c) shows an OM image of 2D single crystalline $HfSe_2$ nanosheets synthesized on a mica substrate, which are obtained by the separated precursor strategy. The $HfSe_2$ nanosheets exhibit a regular hexagonal geometry with uniform optical contrast and an average domain size of about 6.4 μm. The typical growth results of 2D single crystalline $HfSe_2$ nanosheets are better than the previously reported polycrystalline $HfSe_2$ thin films or vertical small size nanosheets (HfS_2) [34, 41], which are due to the high nucleation sites from high volatilization of low melting point $HfCl_4$. Similarly, the normal precursor mixtures could provide erupt chemical supply, resulting in high nucleation sites for randomly vertical 2D $HfSe_2$ [Fig. S1 of the Electronic Supplementary Materials (ESM)] [34, 39]. Therefore, such a design enables NaCl vapor to continuously interact with HfO_2, promotes the stable volatilization of the metal precursor, and achieves a smooth and continuous supply of reactants, thus facilitating the synmthesis of high-quality lateral epitaxy of 2D $HfSe_2$ nanosheets [43]. Raman spectra of the prepared saples [Fig. 1(d)] were obtained using a 532 nm excitation laser for the identification of $HfSe_2$ nanosheets. The in-plane E_g mode of 146.7 cm^{-1} and the out-of-plane A_{1g} mode of 198.6 cm^{-1} were observed, both of which are in good agreement with previously reported results [31, 41]. Three clear and sharp diffraction peaks at 2θ = 14.4°, 44.2°, and 60.1° that correspond to the (001), (003), and (004) crystal planes of $HfSe_2$ were shown, which matched well with the standard PDF card of the $HfSe_2$ crystals (PDF#01-084-6304), indicating that the grown $HfSe_2$ samples have a 1T-phase structure with specific growth direction [Fig. 1(e)] [33]. Therefore, high-quality 2D $HfSe_2$ thin nanosheets were achieved by the remote alkali halide vapor assisted chemical vapor deposition.

The thickness, domain size, and surface morphology of 2D material have a great influence on its physical properties such as band gap and carrier mobility [11, 36, 44]. Therefore, it is crucial to realize the precise control for achieving large-size and ultrathin 2D single-crystal. Herein, the temperature dependence of growth procedures has been systematically carried out to tune the thickness, domain size, and surface morphology. Figures 2(a)–(e) show the optical images of hexagonal $HfSe_2$ nanosheets grown on mica substrates at different temperatures, in which other growth conditions were kept as argon flow rate of 30 sccm, Se temperature of 280 °C and NaCl temperature of 780 °C. Two obvious growth results trends were observed according to the above optical images analysis. First, the optical contrast of the $HfSe_2$ nanosheets changes from light blue to white and finally to silver-pink with the increased growth temperature, indicating that the thickness of the nanosheets is gradually getting much thicker. This is reflected more clearly in

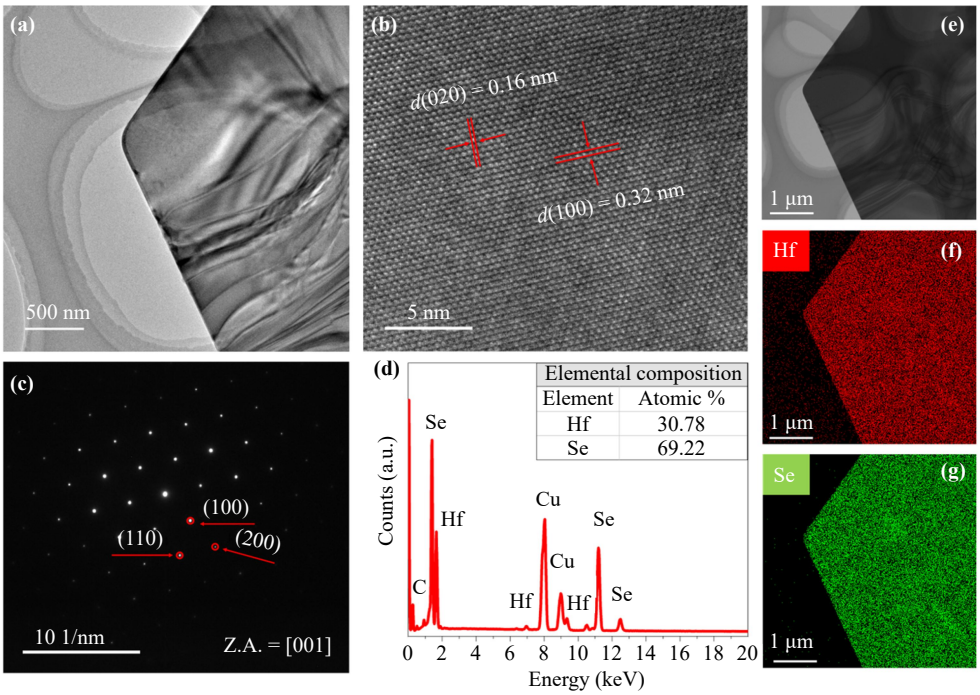

Fig. 3 **(a)** Low-resolution TEM image and **(b)** High-resolution TEM image of 2D $HfSe_2$ nanosheet. **(c)** Corresponding selected-area electron diffraction pattern (SAED). **(d)** EDS elemental analysis spectra of 2D $HfSe_2$ nanosheet and the inset shows the stoichiometric ratio of Hf and Se. **(e)** Dark-field TEM image of 2D $HfSe_2$ nanosheet. **(f, g)** EDS mapping images of Hf and Se, respectively.

the corresponding AFM images [Figs. 2(f–j)] and the thickness statistics histogram [Fig. 2(k)]. The thickness of $HfSe_2$ nanosheets increased from 4.5 to 338.2 nm when the growth temperature was increased from 800 to 940 °C. It is worth noting that 4.5 nm is not the thinnest sample we could obtain, due to the easily oxidizable property of $HfSe_2$ making the samples less than 4.5 nm thick are difficult to measure (Fig. S2 of the ESM). Secondly, the average domain size of $HfSe_2$ nanosheets increases gradually with the increased growth temperature. As shown in Fig. 2(l), the average domain size of $HfSe_2$ nanosheets increased from 6.3 to 20.2 μm when the temperature was increased from 800 to 940 °C. At lower growth temperatures, the low diffusivity of active reactive precursors prefers to bond with the active edge of two-dimensional $HfSe_2$ sheet at the substrate surface, which tends to produce thin two-dimensional $HfSe_2$ nanosheets. As the growth temperature increases, the concentration of active reactants is elevated and the migration rate of precursors on the substrate surface is enhanced, which promote both in-plane and out-of-plane growth of 2D nanosheets, resulting in large and thick materials with lower surface energy. 2D $HfSe_2$ nanosheets grown on SiO_2/Si substrates (Fig. S3 of the ESM) exhibit the similar temperature dependent thickness and domain size regularity. The $HfSe_2$ morphology changes from hexagonal to circular nanosheets and large area thin films were also realized by the tuned ratio of Hf to Se precursor (Fig. S4 of the ESM), and the decreased gas flow rate, respectively (Fig. S5 of the ESM). Thus, the systematic growth results of 2D $HfSe_2$ were carefully explored and shown with high-quality samples under the wide range of synthesis conditions [41, 45].

In order to further investigate the microstructure, elemental composition, and crystallinity of 2D $HfSe_2$ nanosheets, the measurement of transmission electron microscopy was carried out. Vertically grown $HfSe_2$ was pressed directly onto a TEM copper grid for the clean surface quality (Fig. S6 of the ESM). A low-resolution TEM image of a $HfSe_2$ nanosheet exhibited a regular hexagonal corner [Fig. 3(a)]. Figure 3(b) shows the corresponding high-resolution TEM image with the clear lattice stripes showing the excellent crystallinity, in which the lattice spacing of 0.32 and 0.16 nm can be indexed to the (100) and (020) crystal planes of $HfSe_2$, respectively [22]. The selected-area electron diffraction pattern of the $HfSe_2$ nanosheet was shown with regular hexagonal pattern in Fig. 3(c), in which single crystalline diffraction patterns are consistent with the simulated electron diffraction and other electron diffraction from different regions (Fig. S7 of the ESM). Figures 3(f) and (g) show the corresponding elemental mappings of Hf and Se for the samples in Fig. 3(e), in which the Hf and Se elements are uniformly distributed throughout the nanosheets. The elemental analysis spectra of $HfSe_2$

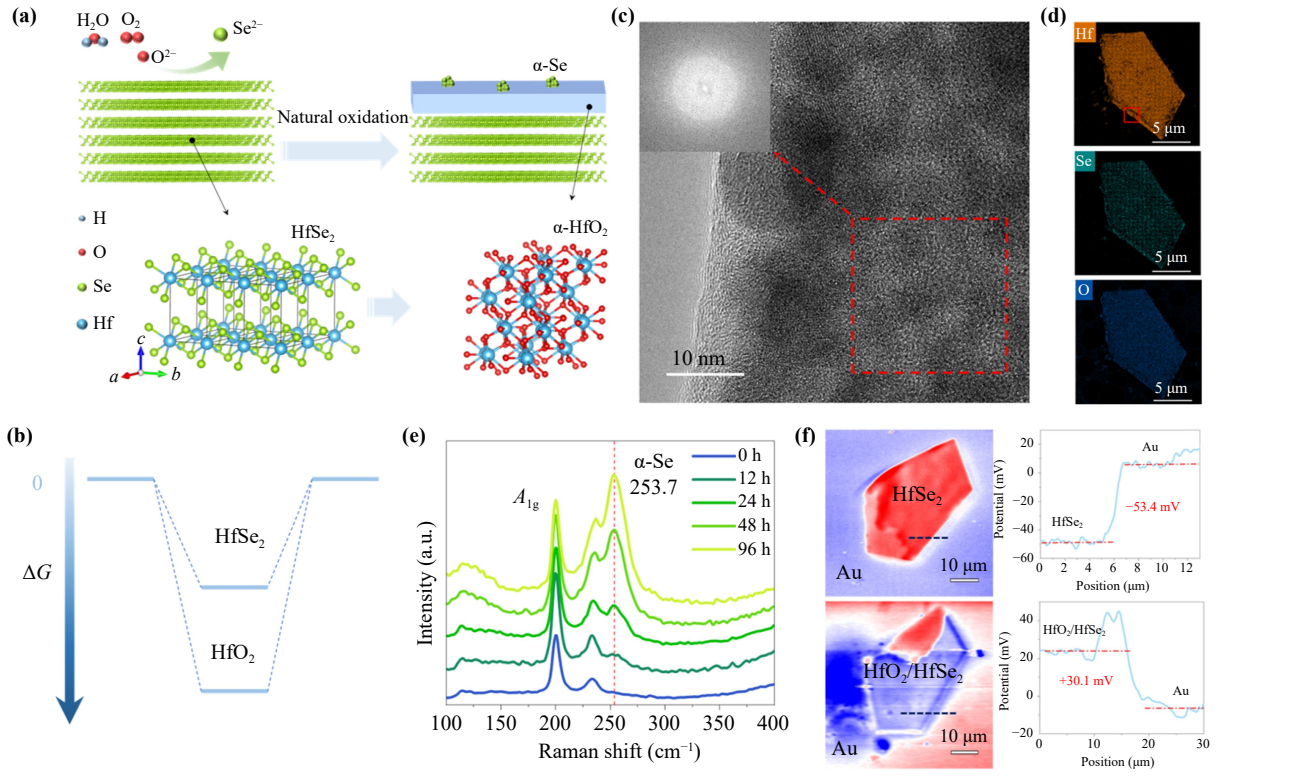

Fig. 4 **(a)** Schematic of natural oxidation of 2D $HfSe_2$ nanosheets in air, forming Se clusters on the surface of HfO_2–$HfSe_2$ heterostructure under the H_2O and O_2 atmosphere. **(b)** Schematic of the relative magnitudes of standard molar Gibbs free formation energies of $HfSe_2$ and HfO_2. **(c)** High-resolution TEM image of $HfSe_2$ nanosheets after 48 h oxidation in air, and the inset image is the corresponding FFT of amorphous HfO_2 structure. **(d)** Corresponding EDS elemental mapping for Hf, Se, and O, respectively. **(e)** Raman spectra of $HfSe_2$ nanosheets naturally oxidized in air for different oxidation times. **(f)** Surface potentials comparison of 2D $HfSe_2$ nanosheets before and after the oxidation.

nanosheets [Fig. 3(d)] indicates that the stoichiometric ratio of Hf to Se is around 1:2.2, which is close to the theoretical chemical ratio.

Thin Hf-based oxide nanostructure or ultrathin film has attracted much interest in recent years, which is highly derisible to develop scalable synthesis methods rather than only relying on atomic layer deposition, etc.. [46] The nonlayered crystal structure and high melting temperature make it difficult to synthesize in large scale 2D forms and get high crystal quality with the cheap semiconductor procedure [47]. Herein, high-quality 2D $HfSe_2$ nanosheets with low Gibbs free formation energy were proposed as the ultrathin template, oxidating into the nonlayered HfO_2–$HfSe_2$ heterostructure, which could be much easier to implement compared to stable 2D HfS_2 [48]. Figure 4(a) illustrates the schematic natural oxidation of 2D $HfSe_2$ in air, where the unstable 2D $HfSe_2$ is exposed to the moist air. The microelectrochemical charge transfer may occur between the material basal plane and the water redox pairs, thus leading to surface oxidation of 2D $HfSe_2$, where the selenium clusters segregate onto the surface of the material in the form of amorphous selenium. The active oxygen atoms could replace the selenium atoms and generate Hf–O chemical bonds, eventually forming the HfO_2–$HfSe_2$ heterostructure or entire HfO_2 amorphous structures. Figure 4(b) shows the relative standard molar Gibbs free energies of $HfSe_2$ and HfO_2, which are much lower for HfO_2 (–1162.4 kJ/mol) than for $HfSe_2$, which confirms the thermodynamical possibility of the transformation of $HfSe_2$ into HfO_2. An air-exposed of ~40 nm $HfSe_2$ nanosheet was used to record Raman spectra at different oxidation time. The optical contrast of $HfSe_2$ nanosheet changes from light blue to dark brown with the increase of exposure time, and there are obvious dark spots appearing on the surface of 2D $HfSe_2$ (Fig. S8 of the ESM). In the time dependent Raman spectrum, it can be seen that after 12 h of natural oxidation, in addition to the representative peaks A_{1g} of $HfSe_2$, a new active peak at 253.7 cm^{-1} appeared [Fig. 4(e)]. This Raman characteristic peak can be indexed as amorphous Se and the peak intensity increases with time. The above results fully confirm that $HfSe_2$ has amorphous Se production during the oxidation process with the maintained Hf–Se chemical bonds. High-resolution TEM images of oxidized $HfSe_2$ nanosheets with corresponding EDS elemental analyses are shown in Figs. 4(c) and (d), respectively. The high-resolution TEM image of oxidized $HfSe_2$

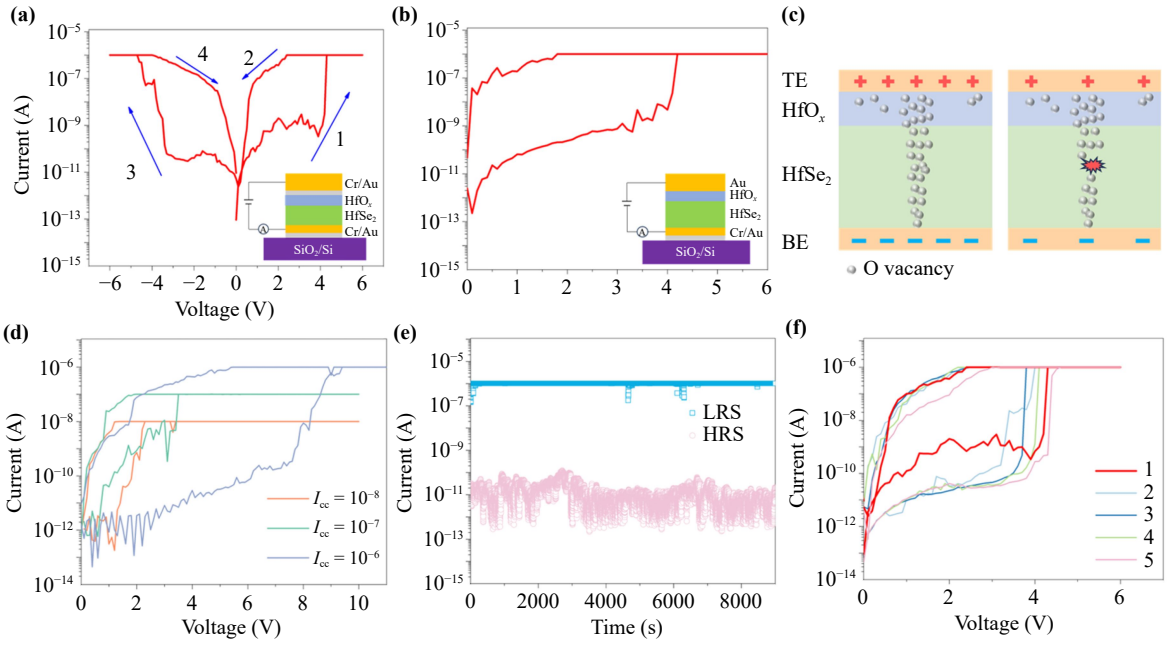

Fig. 5 **(a)** Typical I–V switching curve of the HfO_2–$HfSe_2$ heterostructure memristor with Cr/Au top electrode and Cr/Au bottom electrodes. The inset picture shows the schematic device structure. **(b)** Typical I–V switching curve of the HfO_2–$HfSe_2$ heterostructure memristor with inert Au top electrode and Au bottom electrodes. The inset picture shows the schematic device structure. **(c)** Schematic mechanism diagram of oxygen vacancies dominated resistance change in the HfO_2–$HfSe_2$ heterostructure. **(d)** I–V switching curves of the HfO_2–$HfSe_2$ memristor under different limiting currents. **(e)** Holding characteristics of the high and low resistance states of the HfO_2–$HfSe_2$ memristor. **(f)** The multiple cycling stability measurement of the HfO_2–$HfSe_2$ memristor devices.

nanosheets showed the clear disordered structures with amorphous diffraction rings, indicating the formation of amorphous HfO_2 surface layers [Fig. 4(c)]. The relatively uniform Hf and O elemental mapping and the discrete elemental distribution of weak Se intensities also indicate the chemical oxidation induced by the surface reaction. The unusual FFT diffraction spots of other different regions reveal other specific orientation formation of $HfSe_2$, which may arise the volumetric expansion and lattice strain in the heterostructure (Fig. S9 of the ESM). The surface potential of 2D $HfSe_2$ nanosheets before and after oxidation was measured by the kelvin probe force microscopy, in which the samples were transferred on the gold substrates shown with small roughness change [Fig. 4(f) and Fig. S10 of the ESM]. The surface potential image of HfO_2 layers demonstrated the uniform potential distribution, indicating the slow oxidation kinetics process [Fig. 4(f)]. The surface potential of HfO_2 is higher by 80.5 mV compared to the fresh grown $HfSe_2$, indicating the lowering Fermi level and the decreased electron density [49]. The above results clearly confirm the formation of high-quality HfO_2–$HfSe_2$ heterostructures with the controllable oxidation process.

The vertical memristor devices were constructed by the layer-by-layer transfer and fabrication, using the natural oxidized HfO_2–$HfSe_2$ heterostructure as the active layers [Fig. 5(a)]. A layer of Cr/Au (4/8 nm) was made on the SiO_2/Si surface as the bottom electrode, and the naturally oxidized $HfSe_2$ nanosheets were transferred to the bottom electrode surface. Finally, the top electrode was deposited a layer of Cr/Au (10/70 nm). The characteristic I–V switching curves for this typical memristor were measured by the cyclic voltage scanning in the range 0–6 V with 0.1 V step [Fig. 5(a)]. As the applied positive voltage increases, the device switches from the high-resistance state to the low-resistance state at about 4.1 V. When the voltage drops to 2.3 V, the device spontaneously and gradually switches from the low-resistance state to the high-resistance state. It is possible the surface HfO_2 layer helps reduce lower resistance states of the memristor to obtain a high switching ratio. The symmetrical characteristic I–V relation was also observed for our devices. The CVD derived HfO_2–$HfSe_2$ heterostructure memristor has demonstrated a switching ratio of up to 10^5. In addition, the device could spontaneously and gradually switch from a low-resistance state to a high-resistance state when the external electric field decreases, indicating that the device is volatile, and shown as a threshold switching devices. In order to understand the working mechanism of HfO_2– $HfSe_2$ memristors, the inert metal of Au layers was used as the top and bottom electrodes [Fig. 5(b)]. A significant facile amnesic behavior was observed in several devices [Fig. 5(b) and Fig. S11 of the ESM], in which the immobile

gold atoms inferred oxygen vacancy filament is the main reason of resistance conductivity transition. When a forward bias is applied to the device, the enriched oxygen vacancies in the amorphous HfO_2 layer could gradually move to the bottom electrode. The oxygen vacancies are continuously enriched and migrated, and eventually form a conducting channel across the dielectric layer and show a low resistance state. When the forward voltage decreased, the oxygen vacancy conducting filaments could rupture at the most fragile part, bringing the device back to the high-resistance state [Fig. 5(c)].

The HfO_2–$HfSe_2$ memristor was operated and measured under different limiting currents of 10^{-8}, 10^{-7} and 10^{-6} A, where the device maintained a switching ratio of over 10^3 with a clear memristor windows even the current is as low as 10 nA [Fig. 5(d)]. High device performance at low current density helps to reduce the power consumption of the memristor device and attenuates the adverse effects of high current density on device's lifetime. The hold-up characteristics in the high-resistance and low-resistance states at bias voltages of 3.2 V were measured [Fig. 5(e)]. The measured results showed that the high/low resistive states are virtually unchanged over the experimental time scale of 9000 seconds, indicating that the device is virtually unaffected by read disturbances. The multiple scanning performance of this HfO_2–$HfSe_2$ memristor is shown in Fig. 5(f), demonstrating the voltages window with small fluctuation within two small ranges of 3.8–4.1 V and 2–2.9 V, which indicates the good cycling stability. The relatively high performance and scalable fabrication of HfO_2–$HfSe_2$ heterostructure devices clearly confirm our excellent stable synthesis strategy, which also reveal the oxygen vacancies dominated working mechanism of the memristor.

4 Conclusion

In conclusion, we have successfully and controllably synthesized high-quality 1T-$HfSe_2$ nanosheets on mica and SiO_2/Si substrates using stable molten salt-assisted volatilization of high melting point hafnium-based precursors by chemical vapor deposition. The lateral-size, thickness, and micro-morphology can be precisely adjusted by changing the growth parameters. The high-quality HfO_2–$HfSe_2$ heterostructures were achieved by the easy natural oxidation, in which the selenium clusters segregated onto the surface forming amorphous selenium and oxygen atoms incorporated into $HfSe_2$ lattice replacing the Se atoms. The fabricated HfO_2–$HfSe_2$ heterostructures demonstrated excellent performance of a high switching ratio of 10 [5], and long retention time of over 9000 s under low current density. Our work provides a new synthesis strategy for epitaxy growth of lateral Hf-based layered materials and its heterostructure for high performance scalable electronic devices.

Declarations The authors declare that they have no competing interests and there are no conflicts.

Electronic supplementary materials The online version contains supplementary material available at https://doi.org/10.1007/s11467-024-1414-7 and https://journal.hep.com.cn/fop/EN/10.1007/s11467-024-1414-7.

Acknowledgements This work was financially supported by the National Natural Science Foundation of China (Grant Nos. U23A20570 and 51902346), the Science and Technology Innovation Program of Hunan Province ("HuXiang Young Talents", Grant No. 2021RC3021), the Key Project of the Natural Science Program of Xinjiang Uygur Autonomous Region (Grant No. 2023D01D03), and the Natural Science Foundation of Hunan Province (Grant No. 2021JJ40780). This work was supported by Double Cs-corrected TEM Laboratory of the State Key Laboratory of Powder Metallurgy.

References

1. T. Li, T. Tu, Y. Sun, H. Fu, J. Yu, L. Xing, Z. Wang, H. Wang, R. Jia, J. Wu, C. Tan, Y. Liang, Y. Zhang, C. Zhang, Y. Dai, C. Qiu, M. Li, R. Huang, L. Jiao, K. Lai, B. Yan, P. Gao, and H. Peng, A native oxide high-κ gate dielectric for two-dimensional electronics, *Nat. Electron.* 3(8), 473 (2020)
2. Y. Zhou, D. Wu, Y. Zhu, Y. Cho, Q. He, X. Yang, K. Herrera, Z. Chu, Y. Han, M. C. Downer, H. Peng, and K. Lai, Out-of-plane piezoelectricity and ferroelectricity in layered α-In_2Se_3 nanoflakes, *Nano Lett.* 17(9), 5508 (2017)
3. C. Chen, X. Chen, C. Wu, X. Wang, Y. Ping, X. Wei, X. Zhou, J. Lu, L. Zhu, J. Zhou, T. Zhai, J. Han, and H. Xu, Air-stable 2D Cr_5Te_8 nanosheets with thickness-tunable ferromagnetism, *Adv. Mater.* 34(2), 2107512 (2022)
4. B. Li, Z. Wan, C. Wang, P. Chen, B. Huang, X. Cheng, Q. Qian, J. Li, Z. Zhang, G. Sun, B. Zhao, H. Ma, R. Wu, Z. Wei, Y. Liu, L. Liao, Y. Ye, Y. Huang, X. Xu, X. Duan, W. Ji, and X. Duan, Van der Waals epitaxial growth of air-stable $CrSe_2$ nanosheets with thickness-tunable magnetic order, *Nat. Mater.* 20(6), 818 (2021)
5. X. Fan, R. Xin, L. Li, B. Zhang, C. Li, X. Zhou, H. Chen, H. Zhang, F. OuYang, and Y. Zhou, Progress in the preparation and physical properties of two-dimensional Cr-based chalcogenide materials and heterojunctions, *Front. Phys. 19* (2), 23401 (2023)
6. B. Lei, A. Li, W. Zhou, Y. Wang, W. Xiong, Y. Chen, and F. Ouyang, Room-temperature ferromagnetism and half-metallicity in monolayer orthorhombic CrS_2, *Front. Phys. 19* (4), 43200 (2024)
7. X. Zhu, H. Liu, L. Liu, L. Ren, W. Li, L. Fang, X. Chen, L. Xie, Y. Jing, J. Chen, S. Liu, F. Ouyang, Y. Zhou, and X. Xiong, Spin glass state in chemical vapor-deposited crystalline Cr_2Se_3 nanosheets, *Chem. Mater.* 33(10), 3851 (2021)
8. Y. Zhou, C. Li, Y. Zhang, L. Wang, X. Fan, L. Zou, Z. Cai, J. Jiang, S. Zhou, B. Zhang, H. Zhang, W. Li, and Z. Chen, Controllable thermochemical generation of

active defects in the horizontal/vertical MoS_2 for enhanced hydrogen evolution, *Adv. Funct. Mater.* 33(46), 2304302 (2023)
9. R. Xie, W. Luo, L. Zou, X. Fan, C. Li, T. Lv, J. Jiang, Z. Chen, and Y. Zhou, Low-temperature synthesis of colloidal few-layer WTe_2 nanostructures for electrochemical hydrogen evolution, *Discover Nano* 18(1), 44 (2023)
10. Y. Zhou, J. L. Silva, J. M. Woods, J. V. Pondick, Q. Feng, Z. Liang, W. Liu, L. Lin, B. Deng, B. Brena, F. Xia, H. Peng, Z. Liu, H. Wang, C. M. Araujo, and J. J. Cha, Revealing the contribution of individual factors to hydrogen evolution reaction catalytic activity, *Adv. Mater.* 30(18), 1706076 (2018)
11. Y. Zhou, H. Jang, J. M. Woods, Y. Xie, P. Kumaravadivel, G. A. Pan, J. Liu, Y. Liu, D. G. Cahill, and J. J. Cha, Direct synthesis of large-scale WTe_2 thin films with low thermal conductivity, *Adv. Funct. Mater.* 27(8), 1605928 (2017)
12. Y. Wen, Q. Wang, L. Yin, Q. Liu, F. Wang, F. Wang, Z. Wang, K. Liu, K. Xu, Y. Huang, T. A. Shifa, C. Jiang, J. Xiong, and J. He, Epitaxial 2D PbS nanoplates arrays with highly efficient infrared response, *Adv. Mater.* 28(36), 8051 (2016)
13. G. Wu, L. Xiang, W. Wang, C. Yao, Z. Yan, C. Zhang, J. Wu, Y. Liu, B. Zheng, H. Liu, C. Hu, X. Sun, C. Zhu, Y. Wang, X. Xiong, Y. Wu, L. Gao, D. Li, A. Pan, and S. Li, Hierarchical processing enabled by 2D ferroelectric semiconductor transistor for low-power and high-efficiency AI vision system, *Sci. Bull. (Beijing)* 69(4), 473 (2024)
14. H. Liu, C. Zhu, Y. Chen, X. Yi, X. Sun, Y. Liu, H. Wang, G. Wu, J. Wu, Y. Li, X. Zhu, D. Li, and A. Pan, Polarization-sensitive photodetectors based on highly in-plane anisotropic violet phosphorus with large dichroic ratio, *Adv. Funct. Mater.* 34(17), 2314838 (2023)
15. X. Sun, C. Zhu, J. Yi, L. Xiang, C. Ma, H. Liu, B. Zheng, Y. Liu, W. You, W. Zhang, D. Liang, Q. Shuai, X. Zhu, H. Duan, L. Liao, Y. Liu, D. Li, and A. Pan, Reconfigurable logic-in-memory architectures based on a two-dimensional van der Waals heterostructure device, *Nat. Electron.* 5(11), 752 (2022)
16. J. Zhu, L. Wang, J. Wu, Y. Liang, F. Xiao, B. Xu, Z. Zhang, X. Fan, Y. Zhou, J. Xia, and Z. Wang, Achieving 1.2 fm/$Hz^{1/2}$ displacement sensitivity with laser interferometry in two-dimensional nanomechanical resonators: Pathways towards quantum-noise-limited measurement at room temperature, *Chin. Phys. Lett.* 40(3), 038102 (2023)
17. B. Liu, W. Chu, S. Liu, Y. Zhou, L. Zou, J. Fu, M. Liu, X. Fu, F. Ouyang, and Y. Zhou, Engineering the nanostructures of solution proceed $In_2Se_xS_{3-x}$ films with enhanced near-infrared absorption for photoelectrochemical water splitting, *J. Phys. D Appl. Phys.* 55(43), 434004 (2022)
18. M. Li, H. Sun, J. Zhou, and Y. Zhao, Engineering phonon thermal transport in few-layer $PdSe_2$, *Front. Phys. 19* (3), 33203 (2023)
19. T. Zhu, Y. Zhang, X. Wei, M. Jiang, and H. Xu, The rise of two-dimensional tellurium for next-generation electronics and optoelectronics, *Front. Phys.* 18(3), 33601 (2023)
20. Y. Wang, X. Guo, S. You, J. Jiang, Z. Wang, F. Ouyang, and H. Huang, Giant quartic-phonon decay in PVD-grown α-MoO_3 flakes, *Nano Res.* 16(1), 1115 (2023)
21. S. H. Chae, Y. Jin, T. S. Kim, D. S. Chung, H. Na, H. Nam, H. Kim, D. J. Perello, H. Y. Jeong, T. H. Ly, and Y. H. Lee, Oxidation effect in octahedral hafnium disulfide thin film, *ACS Nano* 10(1), 1309 (2016)
22. M. J. Mleczko, C. Zhang, H. R. Lee, H. H. Kuo, B. Magyari-Köpe, R. G. Moore, Z. X. Shen, I. R. Fisher, Y. Nishi, and E. Pop, $HfSe_2$ and $ZrSe_2$: Two-dimensional semiconductors with native high-κ oxides, *Sci. Adv.* 3(8), e1700481 (2017)
23. W. Zhang, Z. Huang, W. Zhang, and Y. Li, Two-dimensional semiconductors with possible high room temperature mobility, *Nano Res.* 7(12), 1731 (2014)
24. G. Fiori, F. Bonaccorso, G. Iannaccone, T. Palacios, D. Neumaier, A. Seabaugh, S. K. Banerjee, and L. Colombo, Electronics based on two-dimensional materials, *Nat. Nanotechnol.* 9(10), 768 (2014)
25. N. Peimyoo, M. D. Barnes, J. D. Mehew, A. De Sanctis, I. Amit, J. Escolar, K. Anastasiou, A. P. Rooney, S. J. Haigh, S. Russo, M. F. Craciun, and F. Withers, Laser-writable high-κ dielectric for van der Waals nanoelectronics, *Sci. Adv.* 5(1), eaau0906 (2019)
26. L. Yin, K. Xu, Y. Wen, Z. Wang, Y. Huang, F. Wang, T. A. Shifa, R. Cheng, H. Ma, and J. He, Ultrafast and ultrasensitive phototransistors based on few-layered $HfSe_2$, *Appl. Phys. Lett.* 109(21), 213105 (2016)
27. M. Kang, S. Rathi, I. Lee, D. Lim, J. Wang, L. Li, M. A. Khan, and G. H. Kim, Electrical characterization of multilayer $HfSe_2$ field-effect transistors on SiO_2 substrate, *Appl. Phys. Lett.* 106(14), 143108 (2015)
28. M. Kang, S. Rathi, I. Lee, L. Li, M. A. Khan, D. Lim, Y. Lee, J. Park, S. J. Yun, D. H. Youn, C. Jun, and G. H. Kim, Tunable electrical properties of multilayer $HfSe_2$ field effect transistors by oxygen plasma treatment, *Nanoscale* 9(4), 1645 (2017)
29. T. Kang, J. Park, H. Jung, H. Choi, S. M. Lee, N. Lee, R. G. Lee, G. Kim, S. H. Kim, H. Kim, C. W. Yang, J. Jeon, Y. H. Kim, and S. Lee, High-κ dielectric (HfO_2)/2D semiconductor ($HfSe_2$) gate stack for low-power steep-switching computing devices, *Adv. Mater.* 2312747, doi: 10.1002/adma.202312747 (2024)
30. A. L. Hector, W. Levason, G. Reid, S. D. Reid, and M. Webster, Evaluation of group 4 metal bis-cyclopentadienyl complexes with selenolate and tellurolate ligands for CVD of ME_2 films (E = Se or Te), *Chem. Mater.* 20(15), 5100 (2008)
31. R. Yue, A. T. Barton, H. Zhu, A. Azcatl, L. F. Pena, J. Wang, X. Peng, N. Lu, L. Cheng, R. Addou, S. McDonnell, L. Colombo, J. W. P. Hsu, J. Kim, M. J. Kim, R. M. Wallace, and C. L. Hinkle, $HfSe_2$ thin films: 2D transition metal dichalcogenides grown by molecular beam epitaxy, *ACS Nano* 9(1), 474 (2015)
32. K. E. Aretouli, P. Tsipas, D. Tsoutsou, J. Marquez-Velasco, E. Xenogiannopoulou, S. A. Giamini, E. Vassalou, N. Kelaidis, and A. Dimoulas, Two-dimensional semiconductor $HfSe_2$ and $MoSe_2/HfSe_2$ van der Waals heterostructures by molecular beam epitaxy, *Appl. Phys. Lett.* 106(14), 143105 (2015)

33. S. Li, M. E. Pam, Y. Li, L. Chen, Y. C. Chien, X. Fong, D. Chi, and K. W. Ang, Wafer-scale 2D hafnium diselenide based memristor crossbar array for energy-efficient neural network hardware, *Adv. Mater.* 34(25), 2103376 (2022)
34. B. Zheng, Y. Chen, Z. Wang, F. Qi, Z. Huang, X. Hao, P. Li, W. Zhang, and Y. Li, Vertically oriented few-layered HfS_2 nanosheets: Growth mechanism and optical properties, *2D Mater.* 3(3), 035024 (2016)
35. D. Wang, X. Zhang, H. Liu, J. Meng, J. Xia, Z. Yin, Y. Wang, J. You, and X. M. Meng, Epitaxial growth of HfS_2 on sapphire by chemical vapor deposition and application for photodetectors, *2D Mater.* 4(3), 031012 (2017)
36. L. Fu, F. Wang, B. Wu, N. Wu, W. Huang, H. Wang, C. Jin, L. Zhuang, J. He, L. Fu, and Y. Liu, Van der Waals epitaxial growth of atomic layered HfS_2 crystals for ultrasensitive near-infrared phototransistors, *Adv. Mater.* 29(32), 1700439 (2017)
37. W. Li, J. Zhou, S. Cai, Z. Yu, J. Zhang, N. Fang, T. Li, Y. Wu, T. Chen, X. Xie, H. Ma, K. Yan, N. Dai, X. Wu, H. Zhao, Z. Wang, D. He, L. Pan, Y. Shi, P. Wang, W. Chen, K. Nagashio, X. Duan, and X. Wang, Uniform and ultrathin high-κ gate dielectrics for two-dimensional electronic devices, *Nat. Electron.* 2(12), 563 (2019)
38. C. Li, R. Xin, C. Y. Jiao, Z. Zhang, J. Qin, W. Chu, X. Zhou, Z. Li, Z. Wang, J. Xia, and Y. Zhou, Synthesis of hetero-site nucleation twisted bilayer MoS_2 by local airflow perturbations and interlayer angle characterization, *J. Cent. South Univ.* 30(10), 3187 (2023)
39. X. Zhu, L. Wong, X. Fan, J. Zhao, Y. Zhou, and F. Ouyang, Role of the spatial distribution of gas flow for tuning the vertical/planar growth of nonlayered two-dimensional nanoplates, *Cryst. Growth Des.* 22(1), 763 (2022)
40. W. Chu, R. Xin, L. Zou, X. Fan, X. Zhou, C. Li, and Y. Zhou, Synthesis of nonlayered 2D α-Fe_2O_3 nanosheets by ultralow concentration precursor with Se catalysts design, *Phys. Status Solidi R.* 2023, 2300102 (2023)
41. D. Wang, X. Zhang, G. Guo, S. Gao, X. Li, J. Meng, Z. Yin, H. Liu, M. Gao, L. Cheng, J. You, and R. Wang, Large-area synthesis of layered $HfS_{2(1-x)}Se_{2x}$ alloys with fully tunable chemical compositions and bandgaps, *Adv. Mater.* 30(44), 1803285 (2018)
42. Q. Yao, L. Zhang, P. Bampoulis, and H. J. W. Zandvliet, Nanoscale investigation of defects and oxidation of $HfSe_2$, *J. Phys. Chem. C* 122(44), 25498 (2018)
43. F. Cui, X. Zhao, B. Tang, L. Zhu, Y. Huan, Q. Chen, Z. Liu, and Y. Zhang, Epitaxial growth of step-like Cr_2S_3 lateral homojunctions towards versatile conduction polarities and enhanced transistor performances, *Small* 18(4), 2105744 (2022)
44. F. Zhang, Z. Mo, B. Cui, S. Liu, Q. Xia, B. Li, L. Li, Z. Zhang, J. He, and M. Zhong, Bandgap engineering of BiIns nanowire for wide-spectrum, high-responsivity, and polarimetric-sensitive detection, *Adv. Funct. Mater.* 33(49), 2306077 (2023)
45. Z. Mo, F. Zhang, D. Wang, B. Cui, Q. Xia, B. Li, J. He, and M. Zhong, Ultrafast-response and broad-spectrum polarization sensitive photodetector based on $Bi_{1.85}In_{0.15}S_3$ nanowire, *Appl. Phys. Lett.* 120(20), 201105 (2022)
46. H. Chen, X. Zhou, L. Tang, Y. Chen, H. Luo, X. Yuan, C. R. Bowen, and D. Zhang, HfO_2-based ferroelectrics: From enhancing performance, material design, to applications, *Appl. Phys. Rev.* 9(1), 011307 (2022)
47. H. Chen, L. Tang, H. Luo, X. Yuan, and D. Zhang, Modulation of ferroelectricity in atomic layer deposited HfO_2/ZrO_2 multilayer films, *Mater. Lett.* 313, 131732 (2022)
48. S. Lai, S. Byeon, S. K. Jang, J. Lee, B. H. Lee, J. H. Park, Y. H. Kim, and S. Lee, HfO_2/HfS_2 hybrid heterostructure fabricated via controllable chemical conversion of two-dimensional HfS_2, *Nanoscale* 10(39), 18758 (2018)
49. X. Fan, L. Zou, W. Chu, L. Wang, and Y. Zhou, Synthesis of high resistive two-dimensional nonlayered Cr_2S_3 nanoflakes with stable phosphorus dopants by chemical vapor deposition, *Appl. Phys. Lett.* 122(22), 222101 (2023)